

IMPROVING LOCAL ADAPTIVE FILTERING METHOD EMPLOYED IN RADIOMETRIC CORRECTION OF ANALOGUE AIRBORNE CAMPAIGNS

Lâmân Lelégard * Arnaud Le Bris Sébastien Giordano

LASTIG, Univ Gustave Eiffel, ENSG, IGN, F-94160 Saint-Mande, France
(laman.lelegard, arnaud.le-bris, sebastien.giordano)@ign.fr

KEY WORDS: Analogue Photography, Airborne Imagery, Orthophotomosaic, Radiometry, Colorimetry, Hotspot Correction, PCA, Wallis Adaptive Filter, Moran's I, Spatial Auto-Correlation, Mathematical Morphology, Multi-Scale Analysis.

ABSTRACT:

An orthophotomosaic is as a single image that can be layered on a map. It is produced from a set of aerial images impaired by radiometric inhomogeneity mostly due to atmospheric phenomena, like hotspot, haze or high altitude clouds shadows as well as the camera itself, like lens vignetting. These create some unsightly radiometric inhomogeneity in the mosaic that could be corrected by using a local adaptive filter, also named Wallis filter. Yet this solution leads to a significant loss of contrast at small scales. This current work introduces two elementary studies. In a first time, in order to quantify the loss of contrast due to the use of Wallis filter, a simple multi-scale score is proposed based on mathematical morphology operations. In a second time, an optimal window size for the filter is identified by considering some systematic radiometric behaviours in the images forming the mosaic through principal component analysis (PCA). These two elementary studies are preliminary steps leading to a method of radiometric correction combining Wallis filtering and PCA.

1. CONTEXT

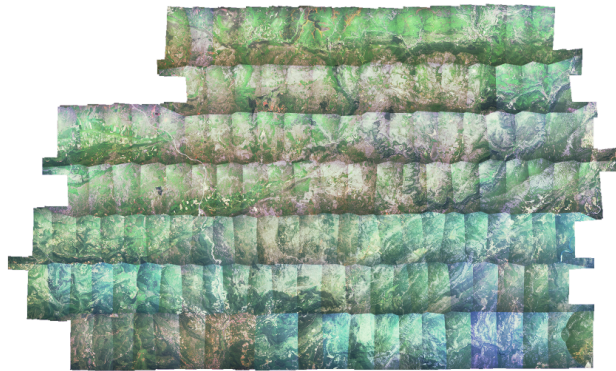


Figure 1. Orthophotomosaic without radiometric correction.

The 143 orthoimages have been computed with the software MicMac (ENSG, 2016, Rupnik et al., 2017) and composing the mosaic displayed on Figure 1 present some radiometric inhomogeneities that seem to follow a similar pattern confirmed by considering the mean of the images as shown on Figure 2. This pattern is due to a combination of several factors: some of them are linked to external parameters, like the hotspot, a sum of retro-specular phenomena caused by the way aerosol and ground are interacting with sunbeams, and some to internal parameters, like the lens vignetting.

Knowing these external and internal parameters for each image of the airborne campaign allows to perform a radiometric correction (Chandelier and Martinoty, 2009). Yet, these parameters are not always available. It is unfortunately the case of the 143 images constituting the dataset of the current study where the lens vignetting or the sun position are unknown. In this case, it is not possible to rely on physical models to perform

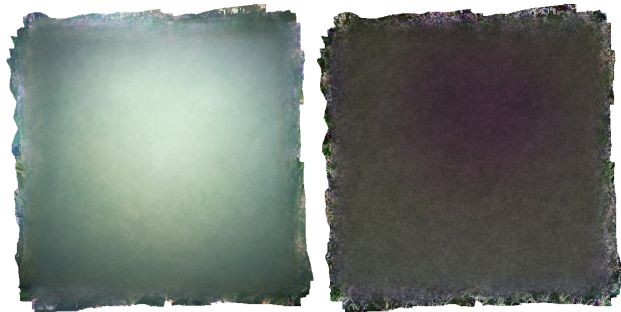


Figure 2. Mean value of the 143 images (left) and of their gradients (right).

radiometric correction. Another method (Wallis, 1976) is then applied consisting of giving locally the same mean and the same standard-deviation, which is the definition of Wallis filtering:

$$Img'(x, y) = \frac{\sigma_0}{\sigma_w(x, y)} \cdot (Img(x, y) - \mu_w(x, y)) + \mu_0 \quad (1)$$

where $\mu_w(x, y)$ and $\sigma_w(x, y)$ are respectively the mean and the standard-deviation computed on the pixel values of the image Img contained in a $w \times w$ pixels square centred on (x, y) . μ_0 and σ_0 are respectively the desired mean and standard-deviation.

In practice, <https://remonterletemps.ign.fr> (IGN, 2016), a governmental French website releasing, among other geographical data, orthophotomosaic of the whole country from different dates in order to show evolution of the lands, displays both recent orthophotomosaics, where the radiometry is corrected using physical method, and old ones corrected by Wallis filtering. A screenshot of the website shown on Figure 3 illustrates the loss of contrast caused by Wallis filtering at small scales.

* Corresponding author.

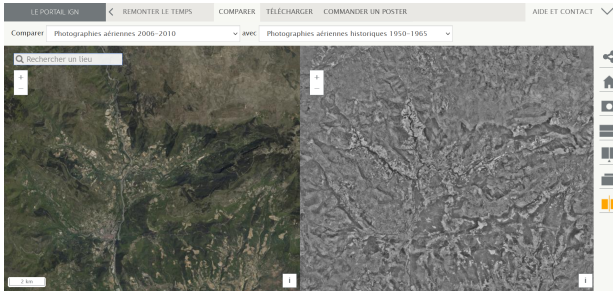


Figure 3. Screenshot of the website
<https://remonterletemps.ign.fr>

The next part of the work introduces a multi-scale score differentiating these two behaviours.

2. MULTI-SCALE ANALYSIS

The experiment is quite basic: the same location is considered on both orthophotomosaics, at different scales (7 in the following example). The 14 level of greys orthoimages are thresholded to obtain binary images with half white and half black pixels. The score, for an image, i.e. a correction at a given scale, is defined as the proportion of pixel, in the binary image, that are invariant by opening and closing in the sense of mathematical morphology. In the presented case, the structuring element is a square window of 3, 5 and 7 pixels displayed respectively in the layer red, green, and blue of the invariant map shown as part of Figure 4.

The curves or Figure 4 seems to suggest that the multi-scale score defined here is decreasing for small scales in the case of a Wallis filtering radiometric correction whereas it stays almost constant for physical corrections. To confirm this observation, this multi-scale score is performed on the 143 images of our dataset and their mean multi-scale scores are displayed for each Wallis filtering size in the Figure 5.

The influence of the Wallis filter size is double: it has an influence on small scales, where the large binary area are vanishing but also on big scales where the proportion of invariant pixels are getting less while the filtering size gets smaller. Eventually, one should insist on the fact that the choice of μ_0 and σ_0 in Wallis filtering has no influence on the binary image (the threshold is the median of the image). The score only depends on the filter size.

A small filter size results into a degradation of the image. This leads to the following question: which is the largest Wallis filtering size that removes hotspot and is the resulting correction acceptable at small scales?

3. PRINCIPAL COMPONENT ANALYSIS

To bring an answer to the previous question, two concepts are introduced: Principal Component Analysis (PCA) and Moran's I. PCA focuses on the systematic behaviours of images (typically, the hotspot) and Moran's I measures the spatial autocorrelation of a phenomenon, or in other words, the behaviour of a variable compared to its neighbours.

The PCA, also known as Karhunen-Loëve transform (Turk and Pentland, 1991), and referred to KLT in the rest of this document, is illustrated by the Figure 6: a set of images, considered

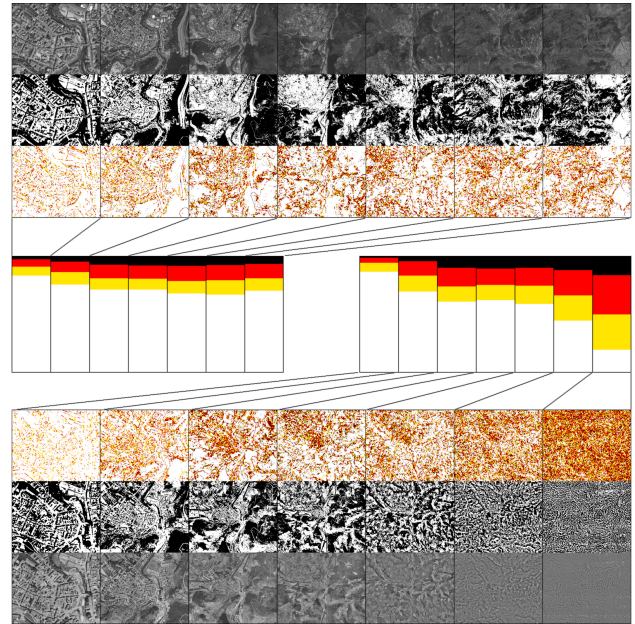


Figure 4.
From left to right, orthophotomosaics of the same location considered at decreasing scales.

On the top, images from 2006-2010 corrected with physical method. On the bottom images from 1950-1965 corrected with Wallis filtering.

In the middle, their respective multi-scale scores: in red and brighter, proportion of pixels that are invariant by opening and closing with a 3×3 pixels structuring element, in yellow and brighter, the same with 5×5 and in white, with 7×7 .

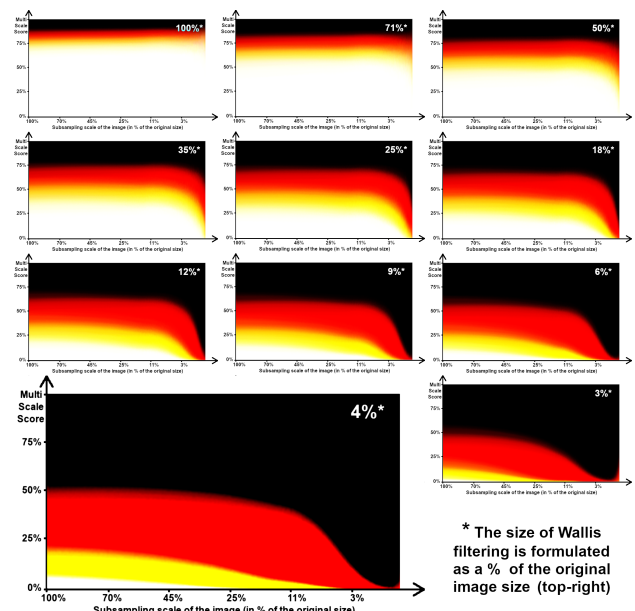


Figure 5. Influence of Wallis filtering on the multi-scale scores of the 143 images dataset.

as vectors of same dimension, are decomposed into eigen images (associated to eigen values) that form a basis. The first vectors of the KLT basis are related to the main behaviours of the image set. In order to apply this transform to our set, each image is cropped to have the same size. Yet an issue appears

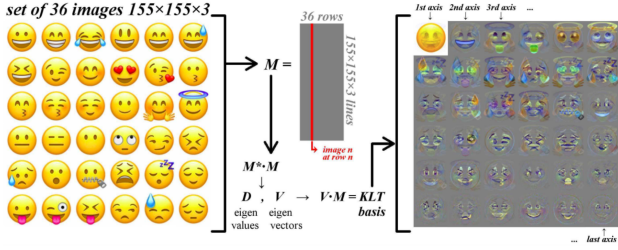


Figure 6. Karhunen-Loève transform.

after performing the KLT: the eigen images (Figure 7) are focusing the border masks of the images more than on the image content. In order to avoid this, an extrapolation of image values is performed on the border masks. The resulting eigen vectors (Figure 8) are no more disturbed by the images border masks.

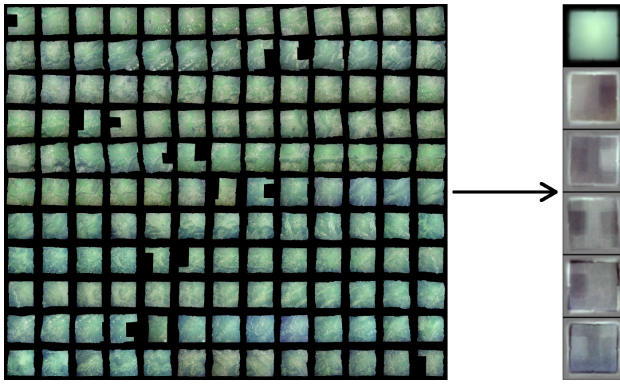


Figure 7. Six first eigen images from the KLT performed directly on the 143 images.

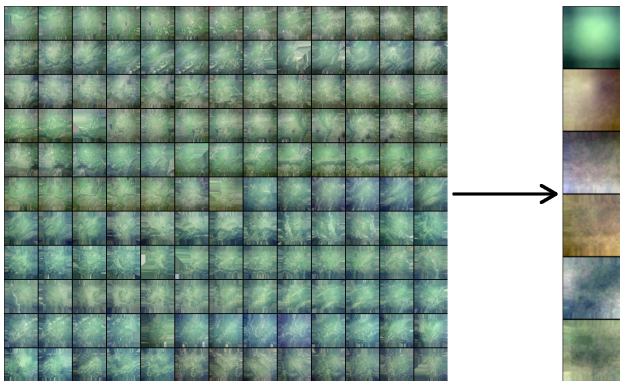


Figure 8. Six first eigen images from the KLT performed on the extrapolated images.

Each image can be reconstructed as a linear combination of the eigen images forming the KLT basis. By construction, the first KLT axis contain most information of images and each eigen image could be interpreted as a pattern shared by several images. By considering the images coefficients for the four first KLT axes as displayed on Figure 9, some spatial correlation seems to occur. The first KLT axes may be interpreted as a systematic and spatially autocorrelated phenomenon (e.g. the hotspot). The following assertion could be made: removing the hotspot with Wallis filtering would have an impact of the coefficients by reducing their spatial autocorrelation.

In order to quantify the spatial autocorrelation of the coeffi-

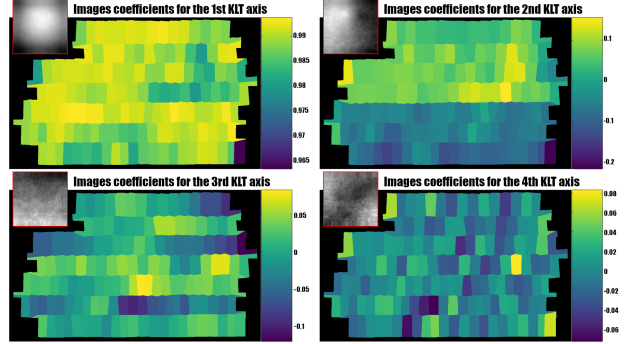


Figure 9. KLT coefficients for each images of the campaign.

cients, Moran's I (Moran, 1950) is computed with the following formula:

$$I = \frac{\sum_{i=1}^N \sum_{j=1}^N p_{ij} \cdot (u_i - \bar{u}) \cdot (u_j - \bar{u})}{\sum_{i=1}^N \sum_{j=1}^N p_{ij} \cdot \sum_{i=1}^N (u_i - \bar{u})^2} \quad (2)$$

where N is the number of images, 143 in this work, u_i the coefficient related to image i , \bar{u} the mean value of the coefficients and p_{ij} the proportion if pixels belonging to i in j (by convention $p_{ii} = 0$). Moran's I could be interpreted the following way: if I is close to $+1$, the spatial correlation is perfect, if I is close to -1 , the spatial dispersion is perfect and if I is close to 0 , the spatial model is random.

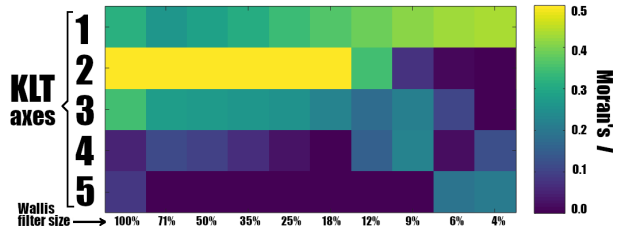


Figure 10. Evolution of Moran's I for different Wallis filter size.

Figure 10 shows the impact of Wallis filter size on spatial correlation of the coefficients. A Wallis filtering with a windows size of 100% of the image is a global contrast and luminosity applied to the whole image. In this case, only the three first KLT axes are showing spatial correlation and may be related to hotspot and vignetting. This spatial correlation seems to vanish for Wallis filter size smaller than 10% of the image size. Yet, as seen previously on Figure 5, this filter size leads to some degradation of the image, more specifically on small scales. To confirm this observation, the resulting orthophotomosaic is displayed on Figure 11.

Hopefully, the results seen in the previous paragraphs may lead to some improvement of Wallis filtering developed in the following section.

4. WALLIS FILTERING IMPROVEMENT

The local mean $\mu_w(x, y)$ and local standard-deviation $\sigma_w(x, y)$ defined in equation (1) could actually be considered as “im-



Figure 11. Orthophotomosaic with basic Wallis filtering correction using optimal window size.

ages” of the same size than the image $Img(x, y)$. For example, $\mu_w(x, y)$ can be considered as $Img(x, y)$ filtered with a square blur of $w \times w$ and $\sigma_w(x, y)$ as the square root of the image $(Img(x, y) - \mu_w(x, y))^2$ filtered by the same $w \times w$ square blur. The computation time of $\mu_w(x, y)$ and $\sigma_w(x, y)$ can be significantly shortened by following a method developed by (Phan et al., 2012) and using the concept of integral images of power m defined as:

$$\overline{Img}^m(x, y) = \sum_{i=1}^x \sum_{j=1}^y Img^m(i, j) \quad (3)$$

The local mean can then be computed from the first order integral image with this formula:

$$\begin{aligned} \mu_{2n+1}(x, y) = & (+\overline{Img}^1(x + n, y + n) \\ & - \overline{Img}^1(x + n, y - n) \\ & - \overline{Img}^1(x - n, y + n) \\ & + \overline{Img}^1(x - n, y - n)) / (2n + 1)^2 \end{aligned} \quad (4)$$

For the local standard-deviation, the formula introduced by (Phan et al., 2012) is:

$$\begin{aligned} \sigma_{2n+1}(x, y) = & (+\overline{Img}^2(x + n, y + n) \\ & - \overline{Img}^2(x + n, y - n) \\ & - \overline{Img}^2(x - n, y + n) \\ & + \overline{Img}^2(x - n, y - n)) / (2n + 1) \\ & - (\mu_{2n+1}(x, y))^2 \end{aligned} \quad (5)$$

The computed local means and the local standard-deviations are then forming two sets of $N = 143$ images each. A KLT is then performed on each set $(\mu)_{1\dots N}$ and $(\sigma)_{1\dots N}$. The $\bar{\mu}^k$ (respectively the $\bar{\sigma}^k$) are defined as the images reconstructed with the k first KLT axes from the set $(\mu)_{1\dots N}$ (respectively the $(\sigma)_{1\dots N}$). In the previous section, it has been shown (Figure 10) that the radiometric distortion caused by the hotspot

and the lenses vignetting is mostly linked to the three first KLT axes. The following assertion will be made: $\bar{\mu}^3$ and $\bar{\sigma}^3$ are only related to systematic phenomena, like hotspot and vignetting, and, therefore, independent from the ground (forest, fields, urban area, etc.). The new correction introduced in the present work, and inspired by Wallis filtering equation (1), is given by the formula:

$$Img''(x, y) = \frac{\sigma_0}{\bar{\sigma}_w^3(x, y)} \cdot (Img(x, y) - \bar{\mu}_w^3(x, y)) + \mu_0 \quad (6)$$

where μ_0 and σ_0 are respectively defined as the image global mean and global standard-deviation.

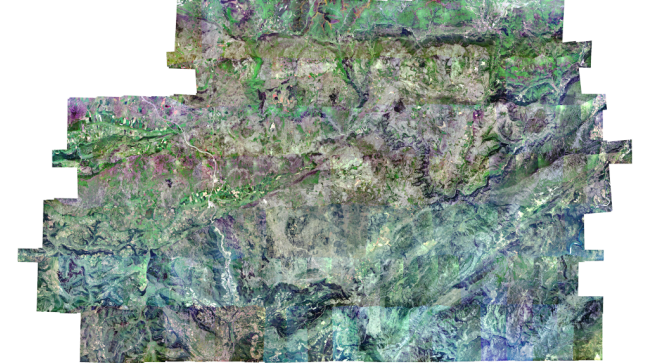


Figure 12. Orthophotomosaic with improved Wallis filtering correction using optimal window size.

The resulting orthophotomosaic is displayed on Figure 12. Compared to Figure 11, the new orthophotomosaic seems to conserve contrast at small scale. This visual observation is confirmed quantitatively with the multi-scale score of the corrected images shown on Figure 13. Compared to the images corrected with basic Wallis filtering (Figure 5: multi-scale score related to a window size of 10%) the images corrected with an improved Wallis filtering shows better multi-scale behaviour.

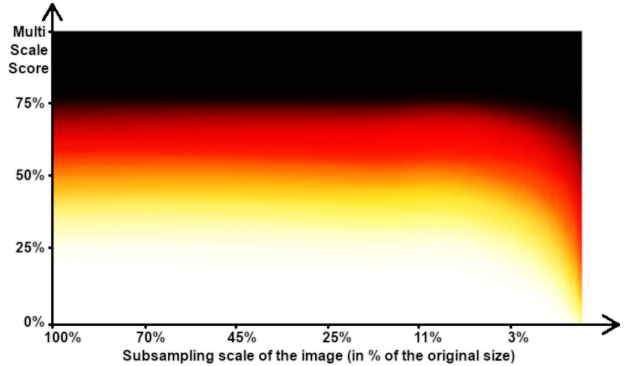


Figure 13. Multi-Scale Score of the 143 images corrected with our improved Wallis filtering.

Yet, a last issue remains, the images do not show the same colour. These inhomogeneities could be caused by several factors, like atmospheric veil or, more likely, some very little variation in the complex chemical process of analogue film developing. In order to remove these colour inhomogeneities, the last section of this work focuses on a simple colour correction method.

5. FINAL EQUALISATION

Figure 14 (top) shows an orthophotomosaic where the images are merged with their overlap: each pixel or this mosaic is the mean of the overlapping images. For each initial image Img , i.e. for each image corrected with the improved Wallis filtering (Figure 14, bottom left), the corresponding image in the mosaic (with overlaps) is extracted and noted Img (Figure 14, bottom right).

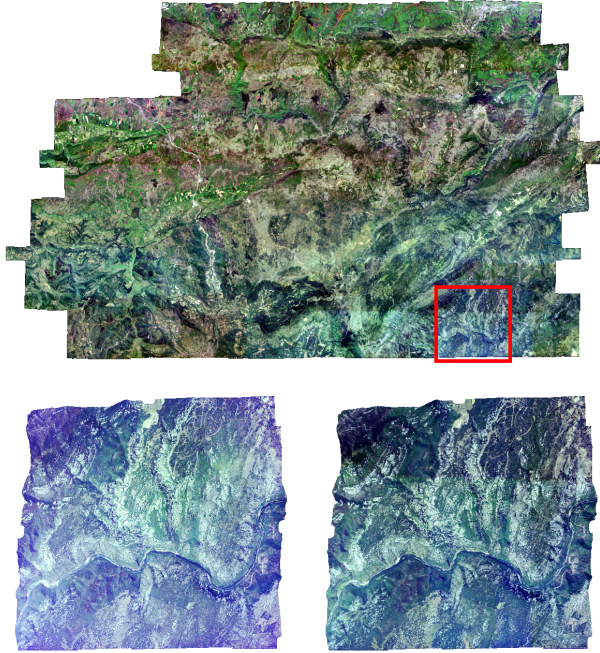


Figure 14. An image and its corresponding image extracted from the orthophotomosaic.

In order to make the initial image look like its equivalent image extracted from the mosaic, a histogram transfer is applied:

$$Img' = CH_{Img}^{-1}(CH_{Img}(Img)) \quad (7)$$

where CH_{Img} is the cumulative distribution function of the histogram of Img or, in other words, $CH_{Img}(v)$ is proportional to the number of pixels of Img having a value smaller or equal to v . CH_{Img}^{-1} is defined as the inverse function of CH_{Img} .

Using the histogram transfer method instead of a simpler one, as for example a global Wallis “filter”, is justified here because of the nature of the analogue images: their response is not linear like a CCD sensor (Litvinov and Schechner, 2005) so a more complex approach may be required. After performing this colour equalisation for all the images, the same step is repeated in an iterative way with the Img' and their corresponding $\widehat{Img'}$. The final result is reached in a few iterations only (Figure 15) and gives a more aesthetic result, at small scales, than the previous approaches (Figures 11 and 12).

6. DISCUSSION

The current work mostly focuses on radiometric correction of orthoimages with the aim of displaying aesthetic orthophoto-

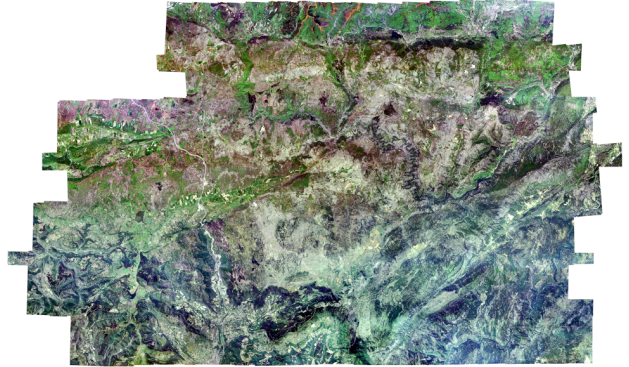


Figure 15. Our final orthophotomosaic.

mosaics. Yet some further experiments are scheduled: as applying the same process directly on raw images in their initial camera geometry (interior orientation) or trying to determine the centre of the hotspot in order to estimate the position of the Sun in the sky.

One undiscussed issue in this work is the fact that, on one hand, the varying sizes of the orthoimages and, moreover, their (large) border mask needs to be managed with a time consuming extrapolation and might even lead to some unknown artefacts. On the other hand, raw images, i.e. in their initial camera geometry, are sharing the same size and the same narrow border mask. In addition, the campaign are usually following the same scheme of acquisition, by band, which may be considered as a new systematic phenomenon. Transposing our approach to this kind of images may lead to some interesting results.

The other issue of our approach is that, even if the resulting corrected images seem better than the ones provided by a simple Wallis filtering, the multi-scale behaviour of our image is still far from the quality provided by physically based corrections. Unfortunately, the metadata needed to perform a physical correction are not available for old campaigns. An ambitious perspective would be to modify our approach in order to guess some of the metadata, like the Sun position, the atmospheric veil, or the camera lenses vignetting and, eventually, perform a physically based correction like it is done on more recent campaign.

To sum up, this work could be considered as the first steps of future studies on the radiometry of analogue images provided by historical campaign and archived in some National Mapping Agencies, or any equivalent organisations, since the late nineteenth century.

ACKNOWLEDGEMENTS

This work was supported by the French National Research Agency under the grant ANR-18-CE23-0025.

REFERENCES

- Chandelier, L., Martinoty, G., 2009. A Radiometric Aerial Triangulation for the Equalization of Digital Aerial Images and Orthoimages. *Photogrammetric Engineering Remote Sensing*, 75(2), 193–200.
- ENSG, 2016. Micmac. <https://micmac.ensg.eu> - link visited on February the 6th, 2020.

IGN, 2016. Remonter le temps. <https://remonterletemps.ign.fr> - link visited on March the 30th, 2022.

Litvinov, A., Schechner, Y., 2005. Addressing radiometric nonidealities: a unified framework. *2005 IEEE Computer Society Conference on Computer Vision and Pattern Recognition (CVPR'05)*, 2, 52–59 vol. 2.

Moran, P., 1950. Notes en continuous stochastic phenomena. *Biometrika*, 37(1-2), 17-23. <https://doi.org/10.1093/biomet/37.1-2.17>.

Phan, T., Sohoni, S., Chandler, D. M., Larson, E. C., 2012. Performance-analysis-based acceleration of image quality assessment. *2012 IEEE Southwest Symposium on Image Analysis and Interpretation*, 81–84.

Rupnik, E., Daakir, M., Deseilligny, M. P., 2017. MicMac – a free, open-source solution for photogrammetry. *Open Geospatial Data, Software and Standards*, 2(14).

Turk, M., Pentland, A., 1991. Face recognition using eigenfaces. *Proceedings. 1991 IEEE Computer Society Conference on Computer Vision and Pattern Recognition*, 586–591.

Wallis, R., 1976. An approach to the space variant restoration and enhancement of images. *Proceedings of the Symposium on Current Mathematical Problems in Image Science*, Monterey, CA, USA.

APPENDIX

Maybe some additional figures in order to reach 6 pages?